



UNIVERSITY OF LEEDS

This is a repository copy of *Effects of anisotropic composite skin on electrothermal anti-icing system*.

White Rose Research Online URL for this paper:
<http://eprints.whiterose.ac.uk/155100/>

Version: Accepted Version

Article:

Shen, X, Liu, X, Lin, G et al. (2 more authors) (2019) Effects of anisotropic composite skin on electrothermal anti-icing system. Proceedings of the Institution of Mechanical Engineers, Part G: Journal of Aerospace Engineering, 233 (14). pp. 5403-5413. ISSN 0954-4100

<https://doi.org/10.1177/0954410019845980>

© IMechE 2019. This is an author produced version of a paper published in Proceedings of the Institution of Mechanical Engineers, Part G: Journal of Aerospace Engineering. Reprinted by permission of SAGE Publications.

Reuse

Items deposited in White Rose Research Online are protected by copyright, with all rights reserved unless indicated otherwise. They may be downloaded and/or printed for private study, or other acts as permitted by national copyright laws. The publisher or other rights holders may allow further reproduction and re-use of the full text version. This is indicated by the licence information on the White Rose Research Online record for the item.

Takedown

If you consider content in White Rose Research Online to be in breach of UK law, please notify us by emailing eprints@whiterose.ac.uk including the URL of the record and the reason for the withdrawal request.



eprints@whiterose.ac.uk
<https://eprints.whiterose.ac.uk/>

Effects of Anisotropic Composite Skin on Electro-thermal Anti-icing System

Xiaobin Shen^{1,*}, Xiaochuan Liu¹, Guiping Lin¹, Xueqin Bu¹ and Dongsheng Wen^{1,2}

¹Laboratory of Fundamental Science on Ergonomics and Environmental Control, School of Aeronautic Science and Engineering, Beihang University, Beijing 100191, China

²School of Chemical and Processing Engineering, University of Leeds, Leeds LS2 9JT, UK

Abstract

To study the effects of anisotropic thermal conductivity of composite aircraft skin on the heat transfer characteristics of electro-thermal anti-icing system, the differential equation of anisotropic heat conduction was established using coordinate transformation of principal anisotropy axis. In addition, it was coupled with the heat and mass transfer model of the runback water film on the anti-icing surface to perform numerical simulation of the electro-thermal anti-icing system. The temperature results of the vertical and cylindrical orthotropic thermal conduction in the rectangular and semi-cylindrical composite skin were consistent with those obtained by the traditional orthotropic model, which verified the anisotropic heat conduction model. The temperature distribution of anti-icing surface agreed well with the literature data, which validated the coupled heat

and mass model of the runback water flow and the anisotropic skin. The anisotropic thermal conductivity of composite skin would make temperature change more gradual, and the effect was more significant where the curvature of the temperature curve was greater. However, the anti-icing surface of the electro-thermal anti-icing system was slightly affected by the anisotropic heat conduction of the multi-layered composite skin.

Keywords

Aircraft icing, Electro-thermal anti-icing, Composite materials, Anisotropic heat conduction, Numerical simulation

1 Introduction

When flying in the cloud with super-cooled water droplets, aircraft would collect the droplets and ice accretion would occur on the outside skin surfaces such as lifting surface, engine intake lip and so on. Aircraft icing is a serious threat to flight safety. It not only destroys the aerodynamic shape which leads to a drop in aircraft lift and an increase in drag, but also causes engine surge and reduces power output¹. According to the NASA statistics, aircraft accidents caused by ice accretion accounted for about 9% of all². To ensure flight safety, ice protection system should be equipped for important surfaces. Based on the differences in the type of energy used, typical ice protection systems mainly include mechanical deicing system, fluid ice protection system³, hot air anti-icing system⁴ and electro-thermal anti-icing/deicing system⁵. The latter two systems are the most widely used for modern aircrafts.

In recent years, due to the inherent advantages like high strength, light weight, good process performance, corrosion resistance and excellent fatigue resistance, composite materials have been widely used in aircraft structure manufacturing⁶. Composite material is a material composed of variety materials, and has various characteristics different from its individual components. The amount of composite materials used in an aircraft and the complexity of composite components have gradually become one of the important indicators to measure the aircraft structural advancement. The proportion of composite materials for Airbus A380 aircraft is 30%, of which carbon fiber composite materials amounts to 32 tons⁷. Composite materials on Boeing B787 account for 50% of the total materials⁸, while the proportion for Airbus A350xwb is 53%.⁹ The extensive use of composite materials brings new problems for aircraft ice protection¹⁰. Since the thermal conductivity of the composite materials is low, coupled with the lower bleed air or no bleed air requirements of the more electric aircraft, the hot air anti-icing system is no longer suitable to use¹¹. With various design performance and convenient heating control ability, the electro-thermal anti-icing system, on the other hand, could meet the anti-icing requirements of the composite skin¹².

Studies on electro-thermal anti-icing system were carried out very early, and great progress has been made in the numerical simulation. The ice accretion and anti-icing software packages represented by LEWICE¹³ and FENSAP-ICE¹⁴ took into account the electro-thermal anti-icing system and verified the simulation results with experimental data. In addition, ANTICE established by Al-Khalil¹⁵ and CANICE¹⁶ used by Morency have also obtained electro-thermal anti-icing results which were in good agreement with the experiment data. Based on the ONERA software, Silva^{17, 18} carried out a series of

numerical simulation studies of the electro-thermal anti-icing system. A water film heat and mass transfer model was established, and verified with the literature results. Mu¹⁹ used a loose coupling method to simulate the unsteady electro-thermal deicing process, and obtained the temperature distributions.

Studies on the design, calculation and experiment of composite electro-thermal ice protection²⁰⁻²² have also been concerned. The anisotropic thermal conductivity of composite aircraft skin was considered and involved in the conduction equation²³. However, the numerical simulation studies were not comprehensive, and less attention was paid to the influence of anisotropic heat conduction of composite materials on electro-thermal anti-icing performance. Composite aircraft skin often contains layers of materials with anisotropic characteristics, so its physical properties might be significantly different in various directions. The traditional orthotropic thermal analysis method could only deal with simple configurations. For complex curved structures like wing skins, the anisotropic principal axis directions do not coincide with the absolute coordinate system and would change with positions. The traditional method could not effectively solve the simulation problem of the electro-thermal anti-icing system with composite materials. The setting of the thermal conductivity in LEWICE¹³ was separated in directions normal and parallel to skin surface for anisotropic effects, but the treatment of the coordinate system was not given. Elangovan²⁴ established the skin heat conduction equation in the surface coordinate system with various thermal conductivities in different directions, but the influences of the anisotropic composite materials were not simulated or analyzed.

In order to calculate anisotropic heat conduction of curved structure and numerically analyze the effects of composite materials on electro-thermal anti-icing system,

coordinate transformation of principal anisotropy axis is used to define the anisotropic thermal conductivity tensor at different skin positions. Combining the anisotropic heat conduction with the mass and energy conservation equations of the runback water film on the anti-icing surface, the thermodynamic model is established and the simulation is conducted for the electro-thermal anti-icing system with composite materials.

2 Numerical simulation model

2.1 Composite anisotropic heat conduction model

According to Fourier's law and the energy conservation, the heat conduction differential equation for the internal solid skin of the electro-thermal anti-icing system could be obtained:

$$\rho c \frac{\partial T}{\partial t} = \nabla \cdot (\mathbf{K} \nabla T) + S \quad (1)$$

where ρ is the density, c is the specific heat, T is the temperature and S is the heat source. When considering anisotropy, the tensor form of the thermal conductivity \mathbf{K} is as follows²⁵:

$$\mathbf{K}_{ij} = k \hat{\mathbf{e}}_{ij} \quad (2)$$

where \mathbf{K}_{ij} is the thermal conductivity matrix element, k is the conductivity and $\hat{\mathbf{e}}_{ij}$ is a matrix. In the two-dimensional case, \mathbf{K} is a tensor with four components, and there are nine components in three dimensions. In the actual situation, composite materials of aircraft skin are processed layer by layer and, therefore, have orthotropic properties. The definition of the thermal conductivity \mathbf{K} only needs to determine the components in the

principal axis directions. Local coordinate system is constructed for each control volume (CV) of composite materials with the principal anisotropy axis taken as the coordinate axis, and the solid heat conduction equation is established on it. Then, the anisotropic thermal conductivity in the absolute coordinate is defined by the coordinate transformation matrix of the local coordinate to the absolute one. Derivation in a three-dimensional case is conducted as follows²⁶.

In the principal axis direction of the local coordinate system, Fourier's law could be expressed as:

$$\begin{bmatrix} q_1^* \\ q_2^* \\ q_3^* \end{bmatrix} = - \begin{bmatrix} K_{11}^* & 0 & 0 \\ 0 & K_{22}^* & 0 \\ 0 & 0 & K_{33}^* \end{bmatrix} \begin{bmatrix} \frac{\partial T}{\partial x_1^*} \\ \frac{\partial T}{\partial x_2^*} \\ \frac{\partial T}{\partial x_3^*} \end{bmatrix} \quad (3)$$

The formula is abbreviated as:

$$\mathbf{q}^* = -\mathbf{K}^* \left[\frac{\partial T}{\partial \mathbf{x}^*} \right] \quad (4)$$

The superscript * in the formula represents the parameters in the local coordinate system, and q_i is the heat flux in the direction of the x_i principal axis.

The anisotropic heat conduction equation in the absolute coordinate system can be expressed as:

$$\begin{bmatrix} q_1 \\ q_2 \\ q_3 \end{bmatrix} = - \begin{bmatrix} K_{11} & K_{12} & K_{13} \\ K_{21} & K_{22} & K_{23} \\ K_{31} & K_{32} & K_{33} \end{bmatrix} \begin{bmatrix} \frac{\partial T}{\partial x_1} \\ \frac{\partial T}{\partial x_2} \\ \frac{\partial T}{\partial x_3} \end{bmatrix} \quad (5)$$

Abbreviated as:

$$\mathbf{q} = -\mathbf{K} \begin{bmatrix} \frac{\partial T}{\partial x} \end{bmatrix} \quad (6)$$

The direction cosine matrix \mathbf{A} is defined between the local coordinate system and the absolute coordinate system. Then the heat flux in the absolute coordinate system can also be calculated by:

$$\mathbf{q} = \mathbf{A} \mathbf{q}^* \quad (7)$$

Meanwhile, the partial differential vectors in the two coordinate systems have the following relationship:

$$\begin{bmatrix} \frac{\partial T}{\partial x_1^*} \\ \frac{\partial T}{\partial x_2^*} \\ \frac{\partial T}{\partial x_3^*} \end{bmatrix} = \begin{bmatrix} \frac{\partial x_1}{\partial x_1^*} & \frac{\partial x_2}{\partial x_1^*} & \frac{\partial x_3}{\partial x_1^*} \\ \frac{\partial x_1}{\partial x_2^*} & \frac{\partial x_2}{\partial x_2^*} & \frac{\partial x_3}{\partial x_2^*} \\ \frac{\partial x_1}{\partial x_3^*} & \frac{\partial x_2}{\partial x_3^*} & \frac{\partial x_3}{\partial x_3^*} \end{bmatrix} \begin{bmatrix} \frac{\partial T}{\partial x_1} \\ \frac{\partial T}{\partial x_2} \\ \frac{\partial T}{\partial x_3} \end{bmatrix} \quad (8)$$

which is

$$\begin{bmatrix} \frac{\partial T}{\partial x^*} \end{bmatrix} = \mathbf{A}^T \begin{bmatrix} \frac{\partial T}{\partial x} \end{bmatrix} \quad (9)$$

Bringing equation (9) and equation (7) into equation (4), the following formula can be obtained.

$$\mathbf{q} = -\mathbf{A} \mathbf{K}^* \mathbf{A}^T \begin{bmatrix} \frac{\partial T}{\partial x} \end{bmatrix} \quad (10)$$

By comparing equation (6) with equation (10), it can be seen that in the absolute coordinate system, the thermal conductivity can be expressed as

$$\mathbf{K} = \mathbf{A} \mathbf{K}^* \mathbf{A}^T \quad (11)$$

Correspondingly, the thermal differential equation can be written as

$$\rho c \frac{\partial T}{\partial t} = \nabla \cdot (\mathbf{AK}^* \mathbf{A}^T \nabla T) + S \quad (12)$$

Therefore, for any position of the composite materials, definition of the equivalent thermal conductivity tensor in absolute coordinate system only needs to determine the local conductivity of the orthogonal principal axis and the direction cosine matrix. The user-defined scalar (UDS) transport framework²⁵ in FLUENT software was used to define the anisotropic heat conduction equation of composite materials, and the discrete solution is obtained by the finite volume solver. For a scalar ϕ in most transport conditions, the transport equation has a similar general form:

$$\frac{\partial \phi}{\partial t} + \frac{\partial}{\partial x_i} \left(F_i \phi - \Gamma \frac{\partial \phi}{\partial x_i} \right) = S_\phi \quad (13)$$

where S_ϕ is the source term, F_i and Γ are the coefficients for the convection term and diffusion term, respectively. Those parameters of the equation can be set by user-defined function (UDF) of FLUENT. In this paper, temperature of composite materials is defined as a scalar, and then the anisotropic thermal conductivity is the diffusion coefficient, while the electric heating power is added to the equation through the source term.

2.2 Runback water thermodynamic model

According to the Messinger model²⁷, the mass conservation equation of the runback water film on the anti-icing surface can be obtained from Figure 1:

$$\dot{m}_{in} + \dot{m}_{imp} = \dot{m}_{evap} + \dot{m}_{out} + \dot{m}_{ice} \quad (14)$$

where \dot{m}_{in} and \dot{m}_{out} respectively are the mass flow rate of runback water flowing into and out of the current CV on the anti-icing surface, \dot{m}_{imp} is the water droplets

impinging rate, \dot{m}_{evap} is the water evaporating rate; \dot{m}_{ice} is the mass flow rate of water freezing into ice when the anti-icing power is insufficient.

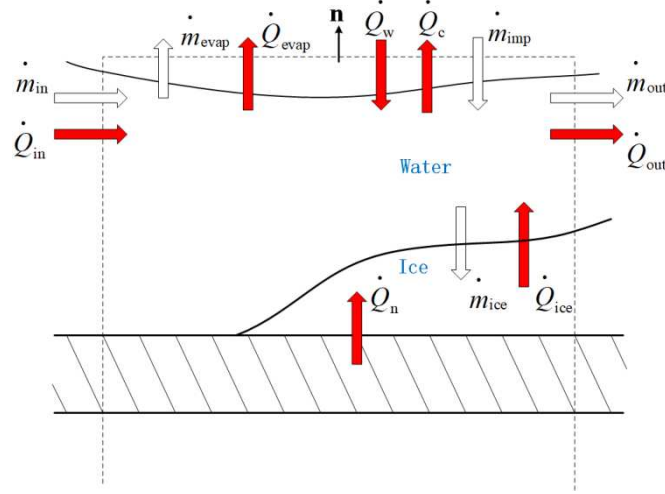


Figure 1. Mass and energy conservation in an anti-icing surface control volume.

As water film runs back along the anti-icing surface, the energy terms flowing into and out of the CV are also shown in Figure 1. \dot{Q}_n is the surface heat flow conducted from internal skin electric heater, \dot{Q}_c is the convective heat flow between water film and air, \dot{Q}_{evap} is the heat flow of water evaporation, \dot{Q}_w is the heat flow of impinging water, and \dot{Q}_{ice} is the heat flow released by the frozen water. \dot{Q}_{in} and \dot{Q}_{out} are the heat flows carried by the runback water inflow and outflow of the CV, respectively. According to the conservation law, energy equation of the runback water film can be expressed as follows.

$$\dot{Q}_c + \dot{Q}_{\text{evap}} + \dot{Q}_{\text{out}} = \dot{Q}_{\text{in}} + \dot{Q}_w + \dot{Q}_n + \dot{Q}_{\text{ice}} \quad (15)$$

where \dot{Q}_n is obtained as follows by solving the differential equation of internal skin anisotropic heat conduction.

$$\dot{Q}_n = K_n \cdot \frac{\partial T}{\partial \mathbf{n}} \cdot \Delta s \quad (16)$$

where \mathbf{n} is the normal vector of the outer skin surface, K_n is the thermal conductivity in the normal direction, and Δs is the surface length of the CV.

\dot{Q}_c is calculated by the convective heat transfer coefficient h_s and the temperature difference.

$$\dot{Q}_c = h_s \cdot (T_s - T_{ad}) \cdot \Delta s \quad (17)$$

where T_s is the anti-icing surface temperature and T_{ad} is the reference temperature calculated under the hypothesis of adiabatic wall.

\dot{Q}_w is composed of the internal energy and the kinetic energy of the impinging water droplets, as expressed as

$$\dot{Q}_w = \dot{m}_{imp} \cdot \left[\frac{U_\infty^2}{2} + c_{p,w} \cdot (T_\infty - T_{ref}) \right] \quad (18)$$

where U_∞ is the flight velocity, $c_{p,w}$ is the specific heat of water, T_∞ is the far field temperature, and T_{ref} is the freezing point temperature of 273.15K. \dot{m}_{imp} can be determined by:

$$\dot{m}_{imp} = \beta \cdot U_\infty \cdot LWC \cdot \Delta s \quad (19)$$

where β is the local collection efficiency, LWC is the liquid water content.

The water evaporative rate \dot{m}_{evap} can be calculated by the Chilton-Colburn analogy method⁵, as expressed below.

$$\dot{m}_{evap} = \Delta s \cdot \frac{h_s}{c_{p,air}} \cdot \left(\frac{Pr}{Sc} \right)^{2/3} \cdot \frac{M_v}{M_{air}} \cdot \left[\frac{p_{v,sat}(T_s) - p_{v,e}}{p_e - p_{v,e}} \right] \quad (20)$$

where $c_{p,air}$ is the specific heat of air, Sc is the Schmidt number, Pr is the Prandtl number, M_v and M_{air} are respectively the molecular masses of water vapor and air,

$p_{v,\text{sat}}(T_s)$ is the saturated vapor pressure at the temperature of T_s . p_e and $p_{v,e}$ are the air pressure and vapor pressure at the edge of boundary layer, respectively.

Meanwhile, \dot{Q}_{evap} is obtained by:

$$\dot{Q}_{\text{evap}} = \dot{m}_{\text{evap}} \cdot i_{lv} \quad (21)$$

where i_{lv} is the latent heat of water evaporation.

\dot{Q}_{ice} consists of the latent heat flow and the sensible heat flow, as expressed as:

$$\dot{Q}_{\text{ice}} = \dot{m}_{\text{ice}} \cdot [i_{ls} + c_{p,\text{ice}} \cdot (T_{\text{ref}} - T_s)] \quad (22)$$

where i_{ls} is the latent heat of water condensation, and $c_{p,\text{ice}}$ is the specific heat of ice.

The solid-liquid state of the runback water film is directly related to the freezing point temperature. According to this constraint, the thermodynamic calculation can be divided into three conditions: above the freezing point, at the freezing point and below the freezing point. Therefore, the results of the CV on the wet anti-icing surface satisfy:

If $T_s > 273.15\text{K}$, there is no ice accretion in the CV, and the runback water remains liquid:

$$\dot{m}_{\text{ice}} = 0 \quad (23)$$

$$\dot{Q}_c + \dot{Q}_{\text{evap}} + \dot{Q}_{\text{out}} = \dot{Q}_w + \dot{Q}_{\text{in}} + \dot{Q}_n \quad (24)$$

If $T_s = 273.15\text{K}$, water and ice are simultaneously present on the anti-icing surface, and the anti-icing surface temperature is known:

$$\dot{Q}_{\text{out}} = 0 \quad (25)$$

$$\dot{Q}_c + \dot{Q}_{\text{evap}} = \dot{Q}_{\text{in}} + \dot{Q}_w + \dot{Q}_n + \dot{Q}_{\text{ice}} \quad (26)$$

If $T_s < 273.15\text{K}$, the runback water in the CV is completely frozen, and there is no

water flowing out:

$$\dot{m}_{\text{out}} = 0 \quad (27)$$

$$\dot{Q}_c + \dot{Q}_{\text{evap}} = \dot{Q}_{\text{in}} + \dot{Q}_w + \dot{Q}_n + \dot{Q}_{\text{ice}} \quad (28)$$

In addition, when there is no water in the CV, it is a dry surface and the heat flow conducted from internal skin is taken away by the external air:

$$\dot{Q}_c = \dot{Q}_n \quad (29)$$

3 Results and Discussion

3.1 Orthotropic Thermal conduction of rectangular segment

The composite skin of an electro-thermal anti-icing system is selected in the open literature, which is used for the validation of ANTICE¹⁵. The multi-layered skin structure consists of six layers as shown in Figure 2, and the material properties of the different layers are listed in Table 1. The electric heating element is insulated by elastomer (COX 4300), and it is closer to the outside surface of the skin. In addition, the outer erosion shield layer is thin and has a high thermal conductivity, while the total thermal resistance of the inner materials is very large. Therefore, more heat energy would be transferred outwards for ice protection, and only a small amount would leak inwards. This multi-layered skin structure is very representative, so the thermodynamic model and the results can be extended to the design of other electro-thermal anti-icing systems.

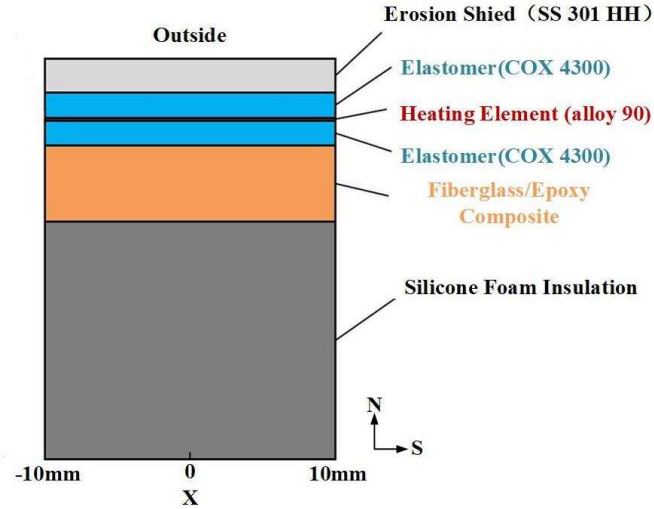


Figure 2. Multilayered skin structure of the electro-thermal anti-icing system.

Table 1. Material properties of the multi-layered skin ¹⁵.

Material	Conductivity (W/m/K)	Density (kg/m ³)	Specific heat (J/kg/K)	Thickness (mm)
Heating Element(alloy 90)	41.018	8906.26	385.112	0.0127
Erosion Shield(SS 301 HH)	16.269	8025.25	502.32	0.2032
Elastomer(COX 4300)	0.256	1383.99	1255.8	0.2794
Fiberglass/Epoxy Composite	0.294	1794.07	1569.75	0.889
Silicone Foam Insulation	0.121	648.75	1130.22	3.429

Firstly, the thermal conduction of a rectangular skin segment is calculated with the width of 20 mm as shown in Figure 2. To analyze the effects of composite materials on the temperature distribution, the anisotropic thermal conductivities of the elastomer and the silicone foam insulation are considered. Based on Tian²⁸, the thermal conductivity ratio between in-plane and through-thickness directions is about 10 for fiber composite materials. Therefore, the thermal conductivities in the normal direction **N** are set with the

data in Table 1, and those in the parallel direction S are 10 times of the normal value. The specific thermal conductivities and calculation cases are listed in Table 2. The inside and outside surfaces of the multi-layered skin are both set as Newman boundary condition with the external temperature of 265.56 K. The convective heat transfer coefficient distribution of the outside skin surface changes with the position in the parallel direction, and it is set to $(150+5000 \cdot X)$ W/K/m², while the value of the inside surface is 10 W/K/m². The side walls of each skin layer are set as adiabatic boundaries. The electric heating power is added as the source term, and the corresponding heat flux is 10 kW/m².

Table 2. Composite thermal conductivities used in different cases.

Material conductivity	case 0	case 1	case 2
Elastomer(COX 4300) (W/m/K)	0.256	0.256	$\frac{0.256(N)}{2.56(S)}$
Silicone Foam Insulation (W/m/K)	0.121	$\frac{0.121(N)}{1.21(S)}$	0.121

Since the heat transfer results of the composite skin are obtained by solving the solid heat conduction differential equation, it is easy to meet the requirements of mesh independence. The contours of temperature for the three cases are listed in Figure 3. It can be seen that the temperature is the highest in the heating elements, and then gradually decreases along the inner and outer sides, reflecting the temperature gradient characteristics of each layer. The inner temperature is higher for the left side than for the right side. This is because the convective heat transfer coefficient outside the left skin is small, and the same heat flux requires a higher temperature to dissipate. From the

comparison of the three conductivity cases, it can also be found that for the temperature in the silicone foam insulation layer, the results of case0 and case2 are consistent but the temperature change of case1 is more gradual with smaller temperature difference. The temperature distributions of the outer materials for case1 and case2 match well, while that for case0 is higher on the left side and lower on the right side.

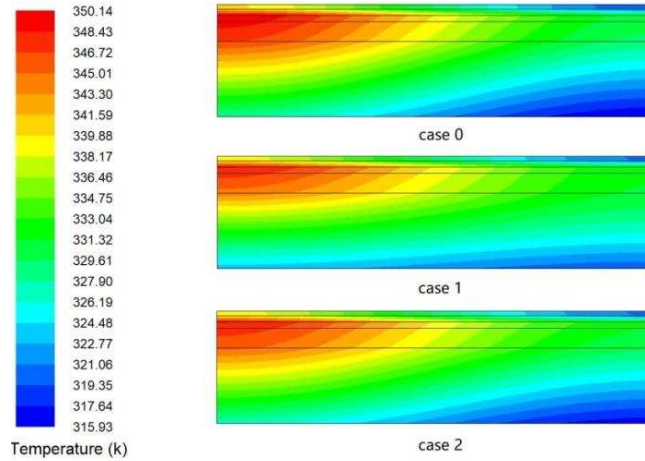


Figure 3. Contour of temperature in rectangular skin segment.

The inside and outside surface temperature curves calculated by the UDS transport equation are compared with the results obtained by the traditional orthotropic calculation model, as shown in Figure 4 and Figure 5. Overall, the inside surface temperature is more affected by anisotropic thermal conductivity than the outside one. From the combinational results of different thermal conductivities, the surface temperature distribution of the inner skin is very non-uniform. Case0 has the largest temperature difference between left and right sidewalls, followed by case2, whereas case1 has the most uniform left-right temperature distribution. The surface temperature difference of the outer skin in Figure 5 is relatively small compared to that of the inner one in Figure 4. The curves of outer skin surfaces for case1 and case2 differ slightly with each other, and are a little more gradual than that for case0.

When the thermal conductivity in parallel direction is larger, the temperature difference between the left and right sidewalls becomes smaller. In addition, since the inside skin surface is the boundary of the silicone foam insulation, the influence of the anisotropic conductivity in case1 directly affects the inside surface and causes its temperature change significantly. The temperature distributions obtained in this paper are completely consistent with the results of the orthotropic model, which validates the anisotropic thermal conduction model with the coordinate transformation method of principal anisotropy axis for orthotropic flat composite material segment.

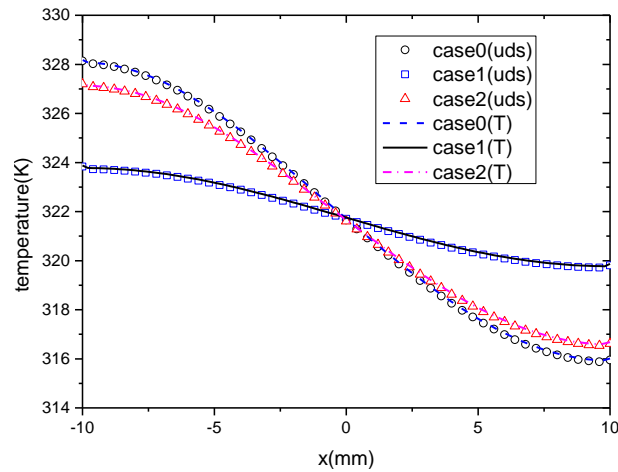


Figure 4. Temperature distribution of the inside skin surface for rectangular segment.

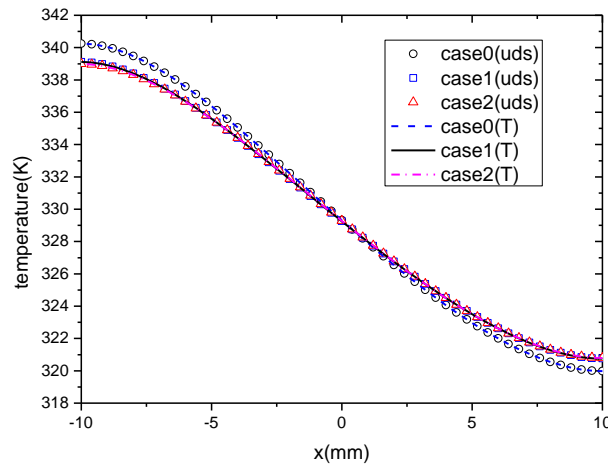


Figure 5. Temperature distribution of the outside skin surface for rectangular segment.

3.2 Cylindrical orthotropic thermal conduction of semi-cylinder

The above-mentioned multi-layered composite skin is used for the electro-thermal anti-icing analysis of a semi-cylindrical model with the diameter of 10.16 cm, as shown in Figure 6. Air flows through the semi-cylindrical skin with super-cooled droplets impinging on the outside surface, and the composite electro-thermal anti-icing structure is arranged in the windward skin. The thermal conductivities of composite materials are the same with those in Table 2. The electric heating layer is divided into four elements, and the radian corresponding to each element is 22.5 degrees. From the leading edge to the downstream, the anti-icing heat fluxes of the heating elements are 30 kW/m^2 , 15 kW/m^2 , 10 kW/m^2 and 10 kW/m^2 , respectively. In addition, the air-droplet flow boundary conditions are as follows: the far-field velocity is 44.7 m/s , the ambient temperature is -7.6°C , the liquid water content is 0.78 g/m^3 , and the water droplet diameter is $20 \mu\text{m}$.

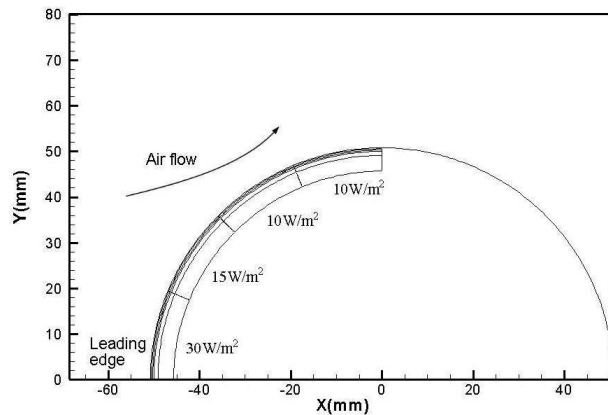


Figure 6. Geometry and heating element arrangement of Semi-cylinder.

The external flow field and the temperature field are obtained by solving the Navier-Stokes(N-S) equations with the Spalart-Allmaras(S-A) turbulence model. The flow field mesh around the cylindrical surface is very fine and the maximum y^+ is smaller than 1, which satisfies the requirements of the mesh independence and the S-A turbulence model

for capturing the boundary layer data accurately. The motion of the super-cooled water droplets and the local collection efficiency β are calculated using the Eulerian method¹⁶. Figure 7 presents the convective heat transfer coefficient and the local collection efficiency on the outside surface of the semi-cylinder. The heat transfer coefficient is small near the leading edge, while β is large. As the distance from the stagnation increases, the heat transfer coefficient gradually rises, while β decreases to zero.

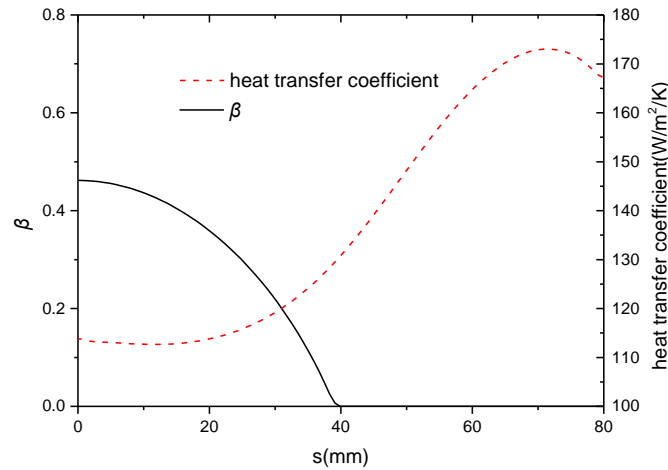


Figure 7. Local collection efficiency and heat transfer coefficient on semi-cylindrical surface.

According to the cylindrical curved structure, the local coordinate system of each grid in the composite material layer is established with the tangential direction as the parallel direction, and then the transformation matrix of that can be obtained. Based on the external air-water flow results, the UDS equation of the anisotropic heat conduction is coupled with the heat and mass transfer model of the runback water film on the anti-icing surface, and the simulation results are presented in Figure 8. It can be seen that the temperatures are very high near the leading edge and gradually decrease as they move backward, which is caused by the larger heating power near the stagnation point. The high temperature area for case1 is more shrinking than those for the other two cases.

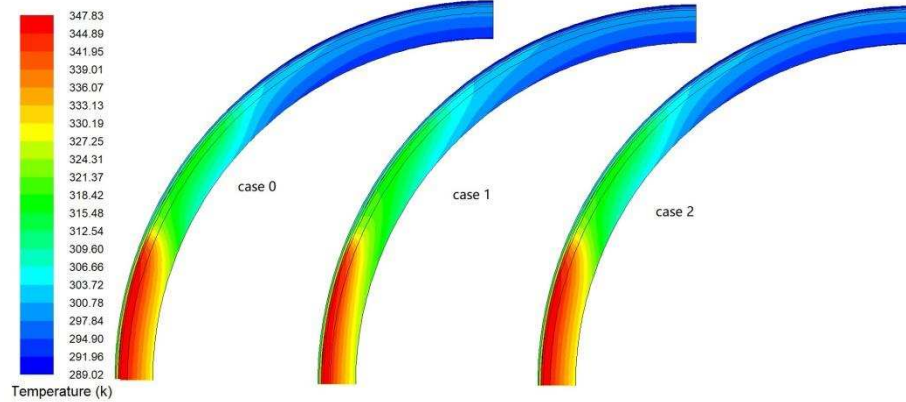


Figure 8. Contour of temperature in semi-cylindrical skin.

The temperature distributions of the inside and outside skin surfaces are compared with the results (T in the Figures) obtained by the cylindrical orthotropic calculation method, as shown in Figure 9 and Figure 10. It can be seen that the temperature results obtained by the two methods show good agreement, which verifies that the anisotropic thermal conduction model based on the coordinate transformation is effective for the heat transfer calculation of the curved composite structure.

It can also be found that the outside temperature in Figure 10 is slightly affected by the anisotropic thermal conductivity for all three cases, while the difference of the inside temperature value in Figure 9 is noticeable only for case 1 which has a narrower temperature range. The temperature distributions of outside surface for the three cases match well with each other, and when the anisotropic thermal conductivity increases, the temperature changes in the parallel direction are a little gentler at the location with greater curvature and higher temperature gradient. It can be explained that due to the high thermal conductivity of the outer erosion shield, the internal temperature deviation can be quickly eliminated. Consequently, the anti-icing temperature of the outside skin surface is also less affected by the anisotropic heat conductivity for the curved semi-cylinder.

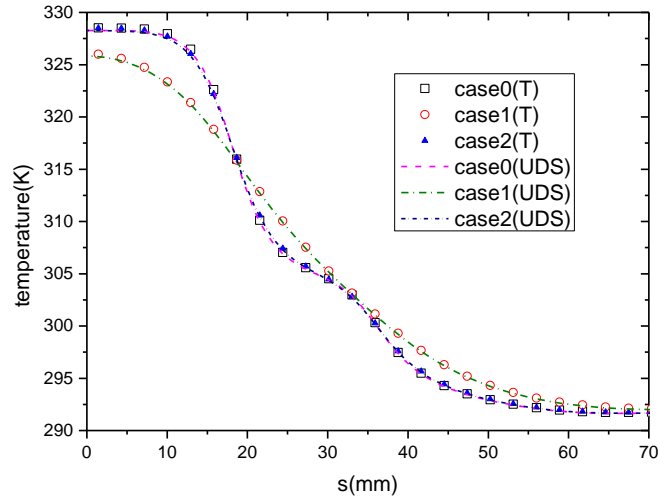


Figure 9. Temperature distribution of the inside semi-cylinder skin surface.

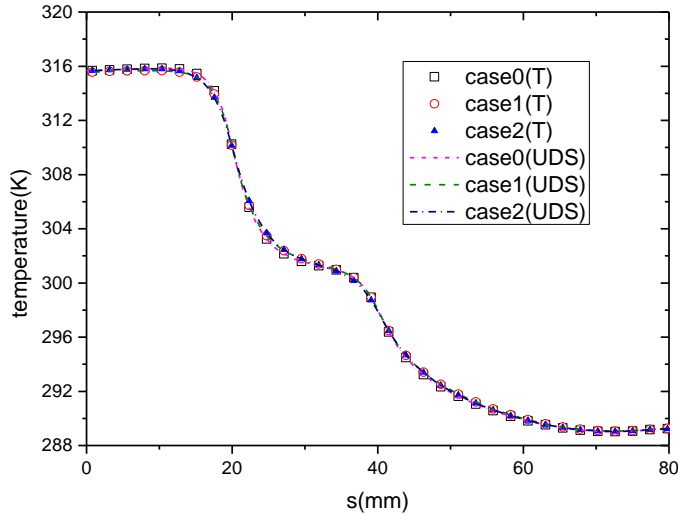


Figure 10. Temperature distribution of the outside semi-cylinder skin surface.

3.3 Anti-icing Characteristics of composite airfoil skin

After verifying the anisotropic heat conduction model, simulation of the electro-thermal anti-icing system and influence analysis of the composite materials are carried out for NACA0012 airfoil with a chord length of 0.9144 m. The representative reference condition, Run 22A, was chosen from Ref.12. The specific flight and icing conditions are the same with those used for the semi-cylinder, and the angle of attack is 0° . The multi-

layered structure and material properties of the skin are consistent with those used in the section 3.1 and 3.2. As shown in Figure 11, there are seven heating elements with different heat fluxes around the leading edge of the airfoil. The start/end position and the heat flux of each element are listed in Table 3, where the dimensionless surface distance $s/c=0$ means the stagnation point. Three cases of different conduction characteristics in Table 2 are simulated to reveal the effects of the anisotropic thermal conductivity.

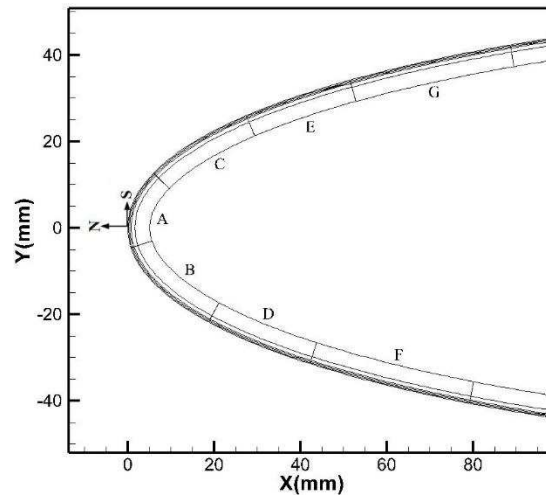


Figure 11. NACA0012 skin internal electro-thermal anti-ice geometry model.

Table 3. Heating strip position and heating heat flux density ¹⁵.

Heating element	Start_s/c	End_s/c	Heat_flux(kW/m ²)
F	-0.1024	-0.0607	9.92
D	-0.0607	-0.0329	10.23
B	-0.0329	-0.0051	32.5
A	-0.0051	0.0157	46.5
C	0.0157	0.0435	18.6
E	0.0435	0.0713	6.98
G	0.0713	0.1129	10.24

The S-A turbulence model is still used for the external airflow and the maximum y^+ is less than 0.3. The convective heat transfer coefficient calculated by N-S equations and the local collection efficiency obtained by the Eulerian method are shown in Figure 12. It can be seen that both results reach their maxima at the stagnation point, and decrease as the distance from the leading edge increases. With those results, the coupling simulation of the internal anisotropic heat conduction and the external heat transfer in the runback water film are performed using the UDS transport equation with UDF according to the local coordinate system defined by the principal axis direction of the solid material layers. Figure 13 presents the anti-icing surface temperature of case 0 compared with the data in the literature¹⁸. Since water droplets impinge on the windward surface, the temperature is low near the leading edge and rises rapidly when all the water evaporates. The result obtained by the coupling model and the UDS approach shows good agreement with the literature data, which verifies the effectiveness of the simulation method for electro-thermal anti-icing systems.

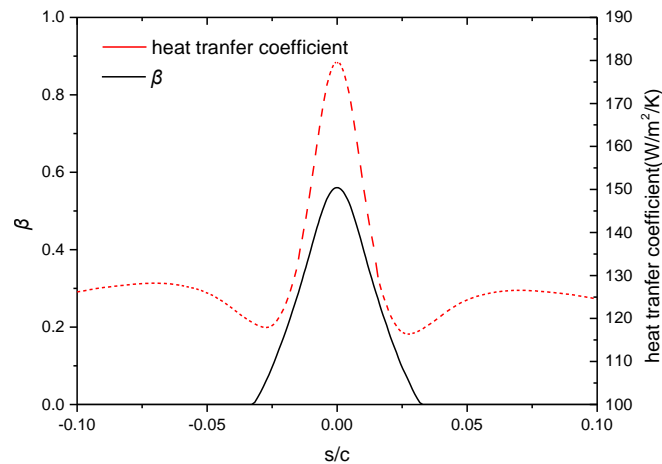


Figure 12. Local collection efficiency and heat transfer coefficient of NACA0012 airfoil.

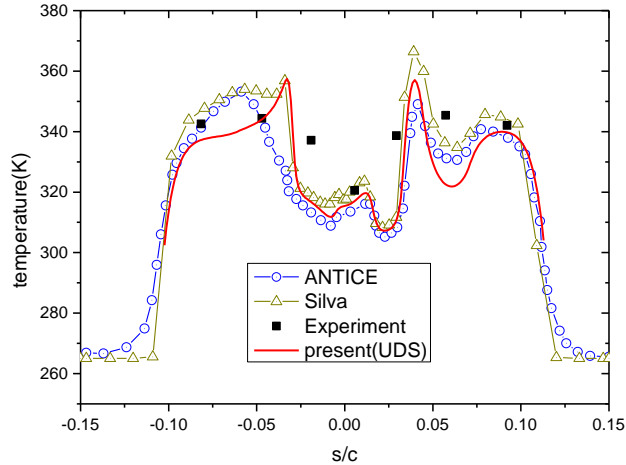


Figure 13. Comparison of surface temperature and literature data.

The temperature contours for the different thermal conductivities are shown in Figure 14. It can be seen that there are several temperature peaks in the multi-layered skin due to the difference heat fluxes of the heating elements. The results for case 0 and case 2 match well, while the temperature change for case 1 is relatively gentle with smaller peak range and higher temperature value in the downstream area. From the temperature distributions of the inside and outside surfaces in Figure 15 and Figure 16, it can be found that the results for case 0 obtained by the UDS equation are almost the same with that from the traditional isotropic differential equation of the heat conduction, which also verifies the effectiveness of the UDS approach.

With gentler temperature changes, the inside surface temperature for case 1 fluctuates less than the other two cases, while the difference between the curves of case 0 and case 2 is not significant. The temperature deviation of the outside surface among the three cases is small, and the differences occur mainly at the greater curvature locations, not just in the temperature peaks or troughs. This phenomenon is the same with the semi-cylindrical results. Firstly, the outer layer of anti-icing skin is always made of metal, and its thermal resistance in parallel direction is small. The variation of heat flux caused by

anisotropy is weakened when conducted through the outer metal layer, and the outside anti-icing surface temperature is slightly affected. Secondly, the surface temperature distribution is determined by the surface heat flux in the normal direction when the external conditions are the same. In the region with greater curvature, the change of the parallel temperature gradient is larger, indicating that a larger amount of energy flows from the normal direction of the layer to the parallel direction. Therefore, when the parallel thermal conductivity becomes larger due to the composite property, the normal heat flux would be redistributed more easily in the parallel direction and the temperature distribution on the surface become gentler. Besides, although the parallel temperature gradient is large, little change of it means that small amount of heat flux flows from the normal direction to the parallel direction, and the influence of anisotropic conductivity is limited.

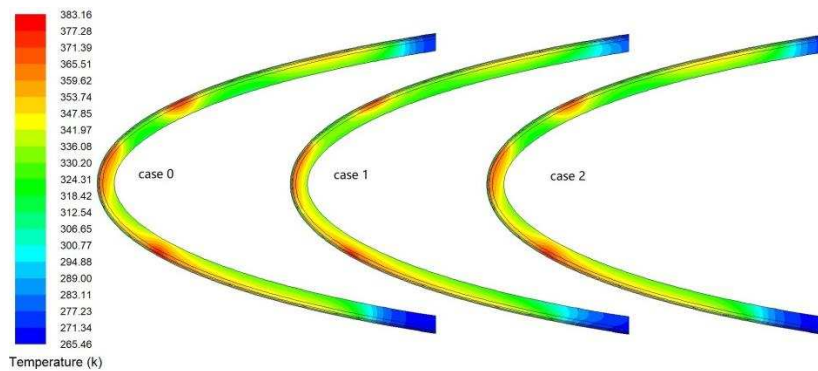


Figure 14. Contour of temperature in NACA0012 airfoil.

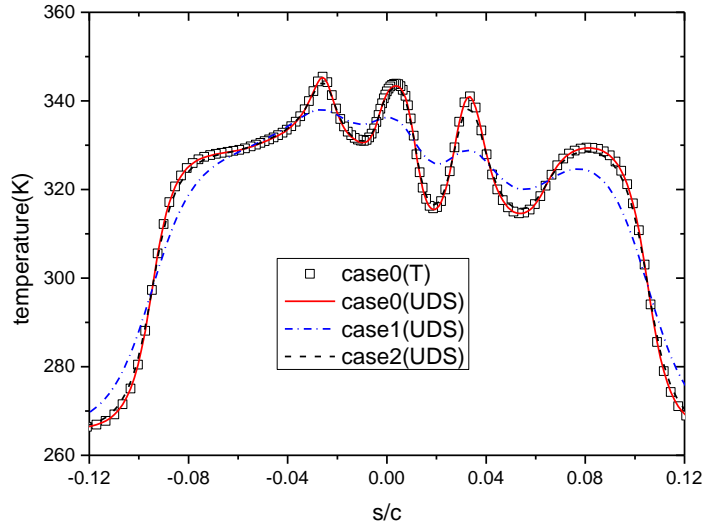


Figure 15. Temperature distribution of the inside airfoil skin surface.

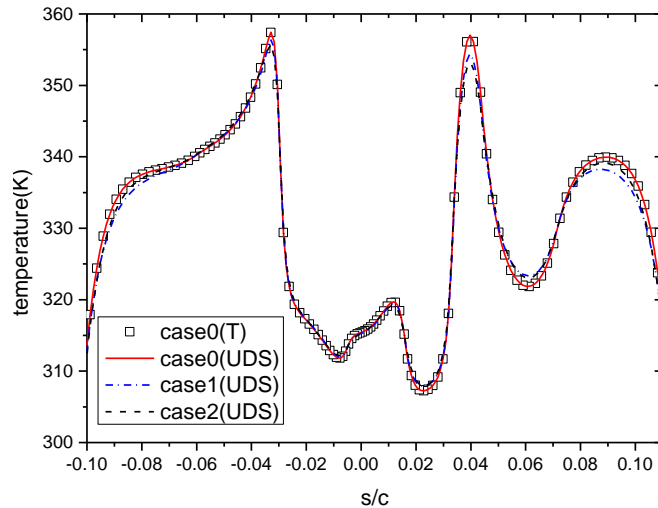


Figure 16. Temperature distribution of the outside airfoil skin surface.

Conclusions

The anisotropic thermal conduction model is established for composite materials, and it is coupled with the runback water thermodynamics to simulate the electro-thermal anti-icing system. The tests on the rectangular and semi-cylindrical composite structures are carried out by the anisotropic heat conduction model with coordinate transformation, and the simulation result of the NACA0012 anti-icing system is compared with the

literature data. Then, the anisotropic effects of the composite materials on electro-thermal anti-icing systems are analyzed, and the main conclusions are as follows:

(1) The temperature distributions of the rectangular and semi-cylindrical composite skins match well with those obtained by the traditional orthotropic model, verifying the anisotropic thermal conduction model for the flat layer and the curved structure.

(2) The simulation result of the NACA0012 electro-thermal anti-icing system is in agreement with the literature data, which verifies the coupled anti-icing model of the solid heat conduction and the heat transfer of the runback water film.

(3) The anisotropic thermal conductivity of composite material makes temperature change gentler and the difference is obvious at the great curvature location. However, the outside anti-icing surface temperature of the electro-thermal anti-icing system is slightly affected by the anisotropic heat conduction.

Funding

This research was supported by the National Natural Science Foundation of China (Grant No. 51806008 and No. 51206008) .

References

1. Heinrich A, Ross R, Zumwalt G. Aircraft icing handbook. Volume 1. *Atlantic City International Airport*, NJ 08405: Department of Transportation, Federal Aviation Administration Technical Center, DOT/FAA/CT-88/8-1.
2. Jones SM, Reveley MS, Evans JK, Barrientos FA. Subsonic Aircraft Safety Icing

Study. NASA/TM-2008-215107, 2008.

3. Afghari MR, Vaziry MA, Mostofizadeh, AR. Computational fluid dynamics investigation of finding appropriate location of fluidic anti-icing protective panel on leading edge of wing. *Proceedings of the Institution of Mechanical Engineers - Part G: Journal of Aerospace Engineering*, 2017; 0(0): 1-12. DOI: 10.1177/0954410017740916
4. Bu XQ, Lin GP, Yu J, Shen XB, Hou PX. Numerical analysis of a swept wing hot air ice protection system. *Proceedings of the Institution of Mechanical Engineers, Part G: Journal of Aerospace Engineering*, 2014; 228(9): 1507-1518. DOI: 10.1177/0954410013494515
5. Bu XQ, Lin GP, Yu G, Yang SH, Song X. Numerical simulation of an airfoil electrothermal anti-icing system. *Proceedings of the Institution of Mechanical Engineers - Part G: Journal of Aerospace Engineering*, 2013; 227(10): 1608-1622. DOI: 10.1177/0954410012463525.
6. Biswas¹ H, Laskar MAR, Shashi GM. Composite and Nanocomposite Materials: Advanced Solutions in Aircraft Construction. *Proceedings of 14th Global Engineering and Technology Conference*; 2017 December 29-30; Dhaka, Bangladesh.
7. Black S. The rear pressure bulkhead for the Airbus A380 employs resin film infusion. *High-Performance Composites* 2003; 11(3): 45-48.
8. Rösner H, Jockel KM. Airbus Airframe-New Technologies and Management Aspects. *Materialwissenschaft Und Werkstofftechnik* 2010; 37(9):768-772.
9. Mrazova M. Advanced composite materials of the future in aerospace industry. *INCAS BULLETIN* 2013; 5(3): 139-150.

10. Ramamurthy P. Nano composites for Aircraft Applications. *Journal of Aerospace Sciences and Technologies* 2014; 66(3): 169-185.
11. Francesco DR. Electrically Heated Composite Leading Edges for Aircraft Anti-Icing Applications [dissertation]. Naples: University of Naples "FEDERICO II"; 2010.
12. Electro-thermal ice protection system for the B-787. *Aircraft Engineering and Aerospace Technology*; 2007; 9(6).
13. Wright WB. User manual for the NASA Glenn ice accretion code LEWICE version 2.2.2. NASA/CR-2002-211793, 2002.
14. Pourbagian M, Habashi WG. Aero-thermal optimization of in-flight electro-thermal ice protection systems in transient de-icing mode. *International Journal of Heat and Fluid Flow* 2015; 54: 167-182. DOI: 10.1016/j.ijheatfluidflow.2015.05.012.
15. Alkhalil K, Horvath C, Miller D, Wright WB. Validation of NASA thermal ice protection computer codes. III - The validation of ANTICE. AIAA paper, no. 97-0051, 1997.
16. Morency F, Tezok F, Paraschivoiu I. Heat and Mass Transfer in the Case of Anti-Icing System Simulation. *Journal of Aircraft* 2000; 37(6): 245-252. DOI: 10.2514/2.2613
17. Silva GAL, Silvares OM, Zerbini EJGJ. Numerical Simulation of Airfoil Thermal Anti-ice Operation, Part 1: Mathematical Modelling. *Journal of Aircraft* 2007; 44(2):627-633. DOI: 10.2514/1.544.
18. Silva GAL, Silvares OM, Zerbini EJGJ. Numerical Simulation of Airfoil Thermal Anti-ice Operation, Part 2: Implementation and Results. *Journal of Aircraft* 2007; 44(2):634-641. DOI: 10.2514/1.24922.
19. Mu ZD, Lin GP, Shen XB, Bu XQ, and Zhou Y. Numerical Simulation of Unsteady

- Conjugate Heat Transfer of Electrothermal Deicing Process. *International Journal of Aerospace Engineering* 2018. 2018: 1-16. DOI: 10.1155/2018/5362541.
20. Mohseni M, Amirfazli A. A novel electro-thermal anti-icing system for fiber-reinforced polymer composite airfoils. *Cold Regions Science and Technology* 2013; 87: 47-58. DOI: 10.1016/j.coldregions.2012.12.003.
 21. Chen L, Zhang YD, Wu Q. Effect of Graphene Coating on the Heat Transfer Performance of a Composite Anti-/Deicing Component. *Coatings* 2017; 158(7): 1-11. DOI: 10.3390/coatings7100158.
 22. Falzon BG, Robinson P, Frenz S, Gilbert B. Development and evaluation of a novel integrated anti-icing/de-icing technology for carbon fibre composite aerostructures using an electro-conductive textile. *Composites Part A Applied Science & Manufacturing* 2015; 68(2015): 323-335. DOI: 10.1016/j.compositesa.2014.10.023.
 23. Wright WB, Keith TGJ, Dewitt KJ. Numerical analysis of a thermal deicer. AIAA paper, no. 92-0527, 1992.
 24. Elangovan R, Olsen R. Analysis of Layered Composite Skin Electro-Thermal Anti-Icing System. AIAA paper, no. 2008-0446, 2008.
 25. *ANSYS FLUENT User's Guide*. release 18.0. ANSYS, Inc; 2018.
 26. Tu Z, Mao J, Han X. Numerical study of film cooling over a flat plate with anisotropic thermal conductivity. *Applied Thermal Engineering* 2017. 111: 968-980. DOI: 10.1016/j.applthermaleng.2016.09.170.
 27. Messinger BL. Equilibrium temperature of an unheated icing surface as a function of airspeed. *Journal of the Aeronautical Sciences* 2012; 20(1): 29-42. DOI: 10.2514/8.2520.

28. Tian T. Anisotropic thermal property measurement of carbon-fiber/epoxy composite materials [dissertation]. Nebraska: University of Nebraska; 2011.